RESEARCH ARTICLE | JULY 07 2025

Non-contact ultrasound imaging based on sub-terahertz photoacoustic effect and laser vibrometry

Yunao Zheng ; Azumi Maekawa ; Yasuaki Monnai

APL Photonics 10, 076105 (2025)
https://doi.org/10.1063/5.0276093

Non-contact ultrasound imaging based on sub-terahertz photoacoustic effect and laser vibrometry

Cite as: APL Photon. 10, 076105 (2025); doi: 10.1063/5.0276093
Submitted: 16 April 2025 • Accepted: 21 June 2025 •
Published Online: 7 July 2025

Yunao Zheng,[1] Azumi Maekawa,[2] and Yasuaki Monnai[1,2,a)]

AFFILIATIONS

[1] Graduate School of Information Science and Technology, The University of Tokyo, 7-3-1 Hongo, Bunkyo-ku, Tokyo 113-8656, Japan
[2] Research Center for Advanced Science and Technology, The University of Tokyo, 4-6-1 Komaba, Meguro-ku, Tokyo 153-8904, Japan

[a)] **Author to whom correspondence should be addressed:** monnai@star.rcast.u-tokyo.ac.jp

ABSTRACT

Ultrasound imaging is a widely used technique for non-destructive testing and in vivo inspection. However, conventional ultrasound imaging relies on contact-based transducers to generate and detect signals, limiting the applicability of the ultrasound. In this study, we propose an approach to implement fully non-contact ultrasound imaging based on the sub-terahertz photoacoustic effect and laser Doppler vibrometry. Compared to infrared pulse-based laser ultrasound systems, the use of continuous sub-terahertz waves enables ultrasound generation through opaque materials, such as clothing and plastics, and offers further prospects of system integration based on solid-state electronics. We demonstrate that the system can detect minute changes in resonance frequency across different media and is capable of tracking multiple ultrasound reflections through inverse Fourier transform. Furthermore, we present a result of raster scan imaging, showcasing the capability of the system for non-contact ultrasound imaging.

I. INTRODUCTION

Ultrasound imaging is a non-invasive and non-destructive technique used to visualize the interior of objects. Ultrasound signals reflect at boundaries of materials and structures with different acoustic impedances, and the returning signals provide structural and mechanical information about the internal features of the object. Conventional ultrasound imaging is typically based on contact-type transducers[1–3] because acoustic impedance matching is required to efficiently transmit and receive ultrasound, bypassing the mismatch of three orders of magnitude in the acoustic impedance between air and water. This requirement not only limits the applicability of ultrasound imaging but also exerts mechanical forces on the object being imaged, making it unsuitable for wounds, burns, vulnerable skin areas, or fragile objects.

Photoacoustic excitation is a promising method for the non-contact generation of ultrasound. It is based on rapid thermoelastic expansion due to the optical absorption of pulsed or modulated light, producing acoustic signals.[4] Depending on the various absorption spectra of different chromophores in biological tissues,[5–7] altering the wavelength of the light source allows ultrasound waves to be excited in different tissues. For example, near-infrared light is strongly absorbed by hemoglobin, thereby enabling photoacoustic imaging of blood vessels.[8] Other common absorbers investigated in previous studies include but are not limited to melanin, lipids, water, and optical dyes.[9–13] In these studies, pulsed lasers in the visible or near-infrared range are typically employed as the excitation source.[11] An emerging direction in ultrasound imaging is the all-optical laser ultrasound system. These systems, building upon photoacoustic excitation, employ optical sensors, such as laser Doppler vibrometers,[14] interferometers,[15] and Fabry–Pérot cavities,[16] to detect photoacoustic signals. Compared to conventional contact-type sensors, optical detectors are non-contact, offer a broader frequency bandwidth, and provide a higher resolution.[17]

Such systems enable full non-contact ultrasound imaging. Studies have reported the application of laser ultrasound systems on metals,[18] in vitro tissue samples,[17,19–21] and human arms.[22,23]

Recently, terahertz waves have drawn attention as a photoacoustic excitation source for underwater and in vivo applications owing to their high absorption in water. Water has an absorption coefficient of ~70 cm^{-1} at 0.1 THz,[24] which increases to over 500 cm^{-1} at 4 THz.[25] As a reference, the maximum absorption coefficient in the near-infrared region is about 100 cm^{-1} around 1900 nm,[26] placing both in a similar order of magnitude. Beyond the absorption properties, terahertz radiation offers the advantage of low photon energy, rendering it non-ionizing and less destructive to biological samples. In addition, terahertz waves can penetrate materials such as plastics and clothing,[27] making them suitable for through-barrier inspection. Previous studies have explored the generation of photoacoustic pulse signals using terahertz pulses in liquid water[28,29] and soy sauces.[30] More recently, the generation of continuous-wave (CW) ultrasound using modulated CW terahertz waves has been demonstrated in water[31–33] and in human bodies.[34] Compared to pulsed excitation, CW excitation allows compact and cost-effective implementation, as has been discussed in optics.[20,35,36] Although the acoustic pressure produced by CW excitation is significantly lower than pulsed excitation, CW excitation can benefit from lock-in techniques to enhance the signal-to-noise ratio.[20,37] Furthermore, modulation of CW terahertz waves enables the generation of arbitrary acoustic waveforms. However, in previous studies, the detection of the CW photoacoustic signals generated by terahertz sources has relied on hydrophones or microphones, posing limitations due to mechanical contact and also limiting spatial resolution.

In this study, we present a system that combines CW sub-terahertz photoacoustics with laser Doppler vibrometry, enabling fully non-contact ultrasound imaging of aqueous samples. We demonstrate the capability of the system to generate and detect ultrasound waves through the detection of the resonance peak shift in liquid solutions and multiple reflections in a gelatin phantom. Furthermore, we present the imaging result on a gelatin phantom embedded with inclusions. Beyond the flexibility provided by non-contact inspection, the detectability through optically opaque boundaries has the potential to inspire a variety of biomedical and industrial applications.

II. SYSTEM VALIDATION

A. Non-contact detection of ultrasound resonance shifts in bottled solutions

Figure 1 depicts the schematic diagram of the experimental setup. The sub-terahertz wave for photoacoustic excitation is generated based on a frequency multiplier-based system introduced by Ichikawa and Monnai.[34] We used a frequency synthesizer (Frequency Synthesizer, Virginia Diodes, Inc.) to generate microwave signals at 15.66 GHz, which are subsequently multiplied by a factor of six using an amplifier–multiplier chain (AMC-I WR10, Virginia Diodes, Inc.) to 93.96 GHz. The signals are then modulated using a PIN diode switch (Ultrafast modulator, Terasense Group, Inc.) controlled with a function generator (WF1974, NF Corporation) and amplified via a power amplifier (QPN-95043328-H8W04, Quinstar Technology). The sub-terahertz wave is emitted through a horn antenna with a lens (Tsurupica, Pax Co., Ltd.) that has a focal length of 50 mm, delivering an output power of ~1.3 W. The focused sub-terahertz irradiation spot has a diameter of about 12 mm. A 1064 nm CW laser Doppler vibrometer (QUARTET, Sound and Bright) is used to detect the ultrasound signals in samples. The vibrometer operates at an output power of 100 mW, with a noise equivalent surface displacement on the order of 10^{-5} nm/$\sqrt{\text{Hz}}$ and a built-in calibration of 100 mV/nm. The laser sensor head is mounted on a three-axis linear stage (OSMS26-100, OptoSigma) and deflected both horizontally and vertically using a 2-axis gimbal mirror (MR-15-30-G, Optotune) to fine-tune the spot position. The laser vibrometer is connected to a lock-in amplifier (LI5660, NF Corporation) synchronized with the PIN diode modulation for noise reduction.

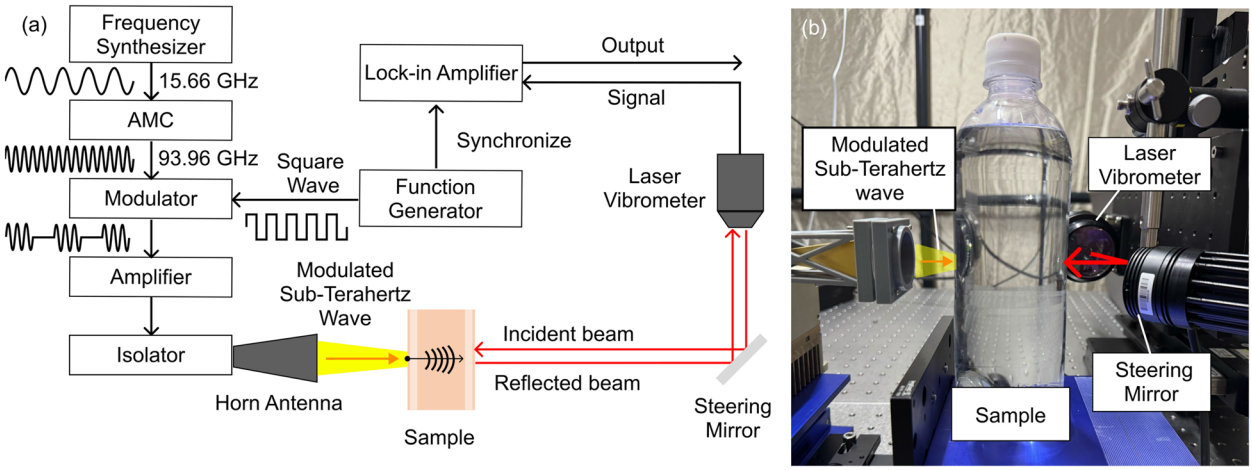

FIG. 1. (a) A block diagram of the system. In this experiment, the transmitter and laser are placed in a transmission configuration. (b) A close-up side view of the measurement process on a sample. The modulated sub-terahertz wave is focused on the sample surface to generate ultrasound within the sample, while the laser is pointed on the opposite side to measure the transmitted wave.

We first conducted experiments using liquid water and normal saline solution. Inspired by the approach of Iravantchi *et al.*,[38] the samples were contained in an off-the-shelf plastic bottle with a diameter of 65 mm and a volume of 580 ml, similar in size and shape to the human forearm. The bottle is placed ~50 mm away from the horn antenna to match the focal length of the lens [Fig. 1(b)]. Sub-terahertz waves are modulated using a square wave signal at 50% duty ratio with a modulation frequency swept from 89 to 94 kHz with a step size of 25 Hz. For each frequency, the modulated sub-terahertz wave is irradiated onto a sample for 0.75 s. We record the lock-in amplifier data with a time constant of 200 ms for each modulation frequency, followed by a 0.75-s pause in irradiation to maintain the sample temperature. A digital thermometer (Sk-270WP-B) with a probe (S270WP-06, Sato Keiryoki Mfg. Co., Ltd.) is used to record the temperature of the sample. The temperature of aqueous samples is 28.5 ±0.1 °C during the experiment. For each sample, the measurement is repeated four times to assess the reproducibility of the results. Before each measurement, the bottle is moved from its original testing position and repositioned.

The measured spectra for the bottled water and saline are shown in Fig. 2. Here, the dots represent the averages across the measurements, and the error bars indicate the corresponding standard errors. Both spectra exhibit clear acoustic resonances, primarily determined by the bottle shape and size. The signal-to-noise ratio of the dominant resonant peak is ~20 dB. Here, we focus on the relative

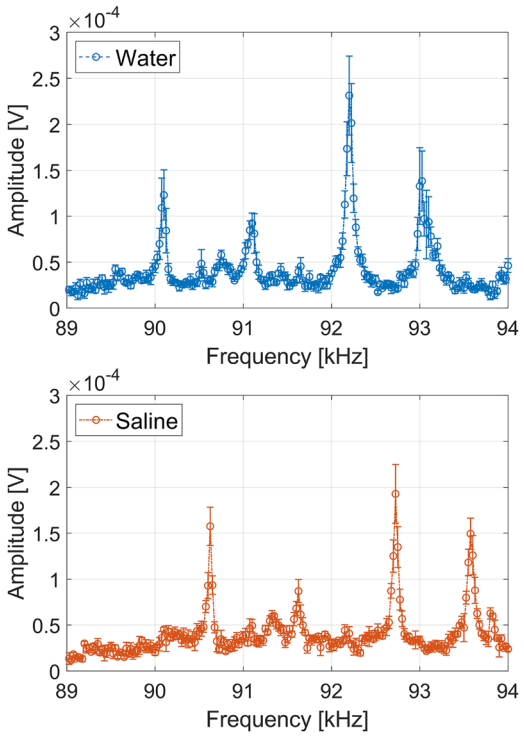

FIG. 2. Average spectrum of water (blue line) and normal saline (red line). The error bar stands for the standard error. The amplitude represents the absolute value of the lock-in amplifier output. The calibration of the laser vibrometer is 100 mV/nm.

shift of the resonance frequencies, which are proportional to sound speed. The resonance peaks appear at 90.100, 91.100, 92.200, and 93.025 kHz for the bottled water, while they appear at 90.625, 91.625, 92.725, and 93.575 kHz for the bottled saline. It can be observed that the two spectra exhibit similar characteristics, and the resonance frequencies of water are consistently 0.58% lower than those of the saline solution. According to the Coppens equation,[39] an empirical formula of the sound speed in salty water is given as

$$c(S,t) = 1449.05 + 45.7t - 5.21t^2 + 0.23t^3 + (1.333 - 0.126t + 0.009t^2)(S - 35), \quad (1)$$

where $t = T/10$ with T in °C and S is the salinity in parts per thousand (ppt). Using this formula, the estimated sound speed is 1505.66 m/s for water and 1515.07 m/s for the saline solution at $T = 28.5$ °C. The difference in sound speed between water and saline is 0.62%, which is consistent with the measurement results obtained from the system.

B. Non-contact broadband ultrasound inspection of gelatin phantoms for temporal feature extraction

Next, we prepare a 6% gelatin-based phantom that models human tissues. Gelatin sourced from porcine and bovine (A-U α, Jellice Co., Ltd.) is used to prepare the sample. We dissolve the gelatin in 50 °C water, after which the mixture is placed in a rectangular mold made of white polypropylene plastic and left in the refrigerator at 4 °C for solidification. The resulting sample [Fig. 3(a)] has a thickness of ~29 mm and is kept at room temperature until it reaches 20 °C before measurement.

The sample is measured using the configuration shown in Fig. 3(b). The laser vibrometer is pointed at the phantom surface, while the sub-terahertz wave is irradiated at the bottom of the container, passes through the white plastic wall, and generates a photoacoustic signal within the phantom. The measurement procedure is conducted following the methodology described in Sec. II A, with a modulation frequency range of 400–1000 kHz and a step size of 0.5 kHz. Figure 3(d) represents the raw frequency domain data, and Fig. 3(e) is the time-domain data obtained using the inverse discrete Fourier transform. Peaks in the time domain are observed at 18.3, 56.7, and 95.1 μs, corresponding to the directly transmitted wave, the first reflected wave, and the second reflected wave,. The estimated sound speed is 1548 m/s, which aligns with the literature value of 1500–1600 m/s[40–42] and matches the typical sound speed of 1550 m/s in human muscle.[42]

The attenuation of the peaks is caused by both the absorption loss and diffraction loss, which is analyzed as follows: The irradiation spot size with a width of 12 mm results in an ultrasound beam with the same width at a central wavelength of 2.2 mm (700 kHz), which keeps collimation within the Rayleigh range and undergoes divergence thereafter. The Rayleigh range is defined by the following equation:

$$L_R = \frac{\pi r^2}{\lambda}, \quad (2)$$

which is $L_R = 51.1$ mm in our case. To estimate the diffraction loss after the Rayleigh range, we model the diffraction process as illustrated in Fig. 3(c), in which we simplify the model by virtu-

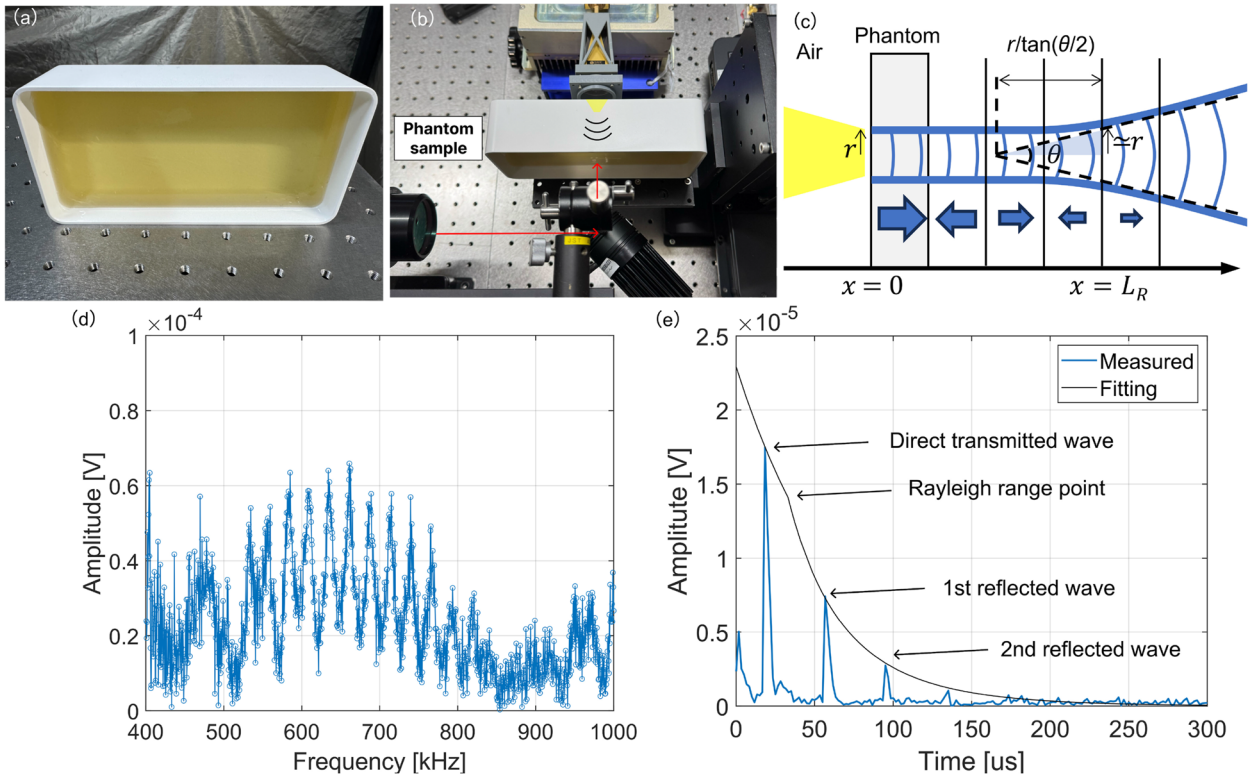

FIG. 3. (a) Gelatin sample prepared for measurement. (b) Experimental setup. (c) A model for the diffraction process. The ultrasound waves reflecting at the air boundary back and forth within the phantom are treated as free-space propagation by virtually removing the boundaries. (d) Frequency-domain data obtained from the measurement. (e) Time-domain data derived using the inverse discrete Fourier transform, with the original data consisting of complex numbers representing phase information.

ally removing the reflective boundaries and assuming free-space propagation. Reflections are represented as occurring at discrete points, shown as vertical lines corresponding to the original boundary locations. Before the Rayleigh range, the beam radius is unchanged from the irradiation spot radius of ~6 mm. After the Rayleigh range, the wavefront diverges with a spreading angle of $\theta = \lambda/2r$. We can assume that this divergent acoustic wave originates from a virtual point source located at the intersection of the extended backline of the divergent wave. Through triangulation, the distance from the virtual point source to the Rayleigh range, where the divergence begins, can be described as $\rho = r/\tan(\theta/2)$. The power attenuation at $x > L_R$ can then be represented by the proportion of the surface area of a sphere with radius ρ to the surface area of a sphere with radius $\rho + (x - L_R)$, where both areas of the sphere share the same solid angle. Since the amplitude is proportional to the square root of the power, the spatial attenuation can be estimated as

$$A = A_0 \cdot \exp(-\alpha x) \cdot \frac{\rho}{\rho + (x - L_R)}, \tag{3}$$

where the exponential component expresses the absorption loss of the material, the fraction component expresses the diffraction loss, x is the travel distance, and α is the attenuation coefficient. Here, the fraction component applies only when x exceeds the Rayleigh range, i.e., $x > L_R$. We perform a least squares fitting using Eq. (3) to obtain the attenuation coefficient; the result is shown in Fig. 3(e). The α is estimated to be 1.18 dB/MHz/cm, consistent with typical attenuation coefficients for water-based phantoms.[42] Thus, we confirm that the proposed approach can attain broadband ultrasound measurement in a non-contact manner through an optically opaque wall.

III. PHANTOM IMAGING

To evaluate the imaging capability of the system, we constructed a 6% gelatin-based phantom embedded with 3D-printed inclusions [Fig. 4(a)] to mimic biological tissue containing regions with varying acoustic impedance. For sample preparation, a base layer of the gelatin phantom is first formed, and 3D-printed letters are placed on its top. Then, an additional 6% gelatin solution at 50 °C is added to completely cover the letters. After the air bubbles are removed, the sample is placed under 4 °C for solidification, keeping the letters centered within the phantom. The letters are 3D-printed using polylactic acid (PLA) with 100% infill. For imaging, the entire sample is translated using a 3-axis linear stage (OSMS26-100, OptoSigma) for scanning. The configuration of the laser vibrometer and the sub-terahertz transmitter is nearly identical to that described in Sec. II B, with minor positional adjustments for fine-tuning. The sample is scanned over a 94 × 52 mm^2 grid with a step of 2 mm.

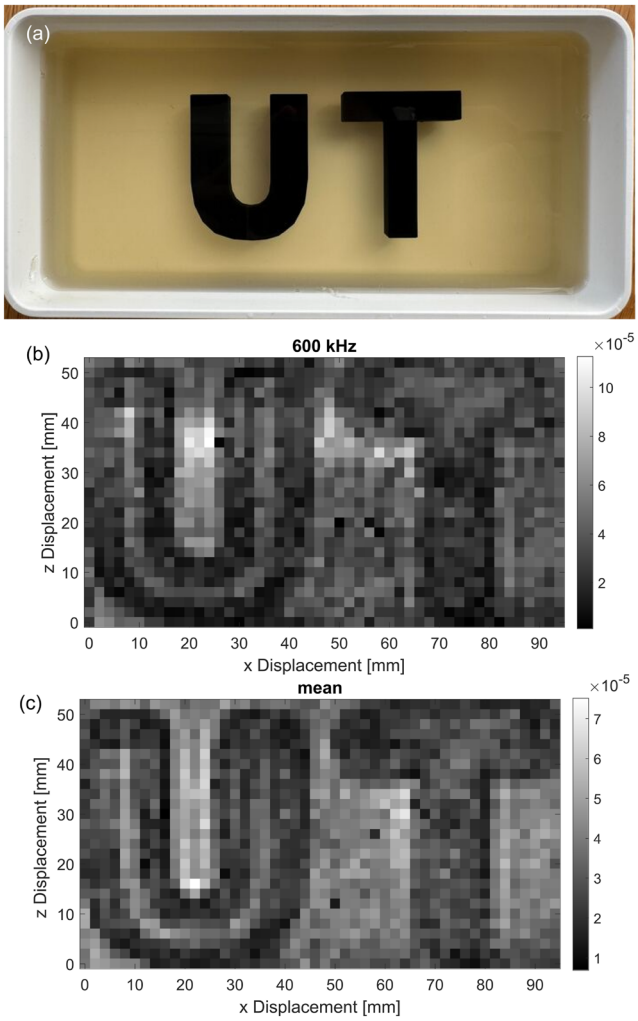

FIG. 4. (a) Phantom sample for imaging capability evaluation. (b) The resulting image at 600 kHz. (c) The resulting image after taking the average of the image of all modulation frequencies.

At each grid point, the modulation frequency is swept from 570 to 600 kHz in 2 kHz intervals, with each frequency applied for 0.2 s. The total scanning time is about 150 min.

The imaging result is shown in Fig. 4. In the experiment, a total of 16 images were obtained for modulation frequencies ranging from 570 to 600 kHz. Here, Fig. 4(b) presents the image at 600 kHz, where the pixel values in the color map represent the amplitude of the lock-in amplifier output. The letter inside the phantom is clearly observed. By averaging the results of the 16 images, we obtained the image shown in Fig. 4(c). The averaging improves the imaging quality, particularly at the boundary between the inclusion and the background phantom.

The imaging resolution in this experiment is influenced by both the sub-terahertz irradiation spot size and the laser spot size. The sub-terahertz irradiation spot has a diameter of ~12 mm, which is significantly larger than the laser spot size (on the order of 100 μm). Therefore, the size of the laser spot plays a dominant role in imaging resolution. On the other hand, sub-terahertz irradiation generates an ultrasound beam propagating with a width of 12 mm. Given that the beam width is comparable to the inclusion sizes, the propagating wave may not only be reflected but also scattered by these inclusions, potentially introducing artifacts in the reconstructed image. It can be noticed that the amplitude in the middle of the letter U is recognizably lower than the adjacent pixels. We infer that this effect may be attributed to the scattered ultrasound wave bypassing the inclusion and forming a constructive interference at the phantom surface. Adjusting the lens to decrease the spot size may help reduce artifacts, but the irradiation power density must be carefully considered to ensure safe exposure for human applications. This can be achieved by adjusting the duty ratio and the irradiation time.[34] According to the Radio Radiation Protection Guidelines defined by the Japan Ministry of Internal Affairs and Communications,[43] for radiation in the frequency range of 30–300 GHz, the maximum permissible exposure of skin is 10 mW/cm^2 averaged within 6 minutes. In our system, the power density at 100% duty ratio is 1150 mW/cm^2. By modulating the irradiation pattern, for example, operating at a 10% duty ratio and limiting cumulative exposure to any skin area to no more than 30 s in 6 min, the time-averaged power density can be reduced to ~9.6 mW/cm^2, thereby complying with the specified safety threshold. The image quality could be further improved by employing appropriate signal processing algorithms.

In future work, we intend to expand the experiment to human subjects. Previous studies have demonstrated the feasibility of directly generating ultrasound beneath the skin using modulated sub-terahertz waves and capturing the signals with a contact microphone for human imaging,[34] as well as detecting photoacoustic signals within the body using a laser vibrometer.[23] These suggest that our system has the potential to serve as a non-contact alternative to conventional contact-based ultrasound sensors for human body measurements. Potential applications include ultrasound-based muscle activity monitoring and non-invasive human imaging. A challenge in human measurement is that the light collection efficiency of optical detection significantly depends on the shape, angle, and reflectivity of the object. However, in practical applications, the reflective properties of the human skin surface are non-uniform, and the directions of reflection and diffraction may dynamically vary due to involuntary movements of the subject, resulting in motion artifacts. This may require the implementation of surface enhancement and adaptive laser steering techniques to ensure that a sufficient signal-to-noise ratio is maintained throughout the measurement process. Furthermore, since the absorption coefficient of water for terahertz waves increases with frequency,[44] using higher frequency terahertz waves allows the generation of higher frequency ultrasound. However, generating terahertz waves at higher frequencies with enough power is still a technical challenge to be developed. Moreover, although this study has focused solely on the transmission mode, we believe that a reflection mode configuration is also feasible, as the signal-to-noise ratio of our system is sufficient to detect ultrasound waves that have undergone multiple reflections [Fig. 3(e)], while typical reflection-mode setups only require detection of waves that undergo a single reflection. We plan to validate this in future work.

IV. CONCLUSION

In this paper, we have presented a system that combines the sub-terahertz photoacoustic effect and laser vibrometry for non-contact ultrasound imaging. Since this system can generate and detect ultrasound signals in aqueous samples without external absorbers, it has the potential to serve as a non-contact alternative to traditional contact-based ultrasonic transducers. Compared to infrared-based laser ultrasound systems, the proposed system offers advantages, particularly in ultrasound waveform customization, through-barrier detection, and system integration. We first demonstrate the capability of the system to generate and detect ultrasound using liquid solutions contained in round plastic bottles and high-water-content gelatin phantoms. Then, we showcase the imaging result of the gelatin phantom that contains inclusions. Future work will involve validation of the reflection mode configuration, in which the transmitter and laser are positioned on the same side, and exploring the application of the system on human subjects, such as non-contact muscle activity monitoring and human imaging.

ACKNOWLEDGMENTS

This work was supported by JSPS KAKENHI 24H00704, JST CRONOS JPMJCS24K3, and Tateisi Science and Technology Foundation (Grant No. 2258002).

AUTHOR DECLARATIONS

Conflict of Interest

The authors have no conflicts to disclose.

Author Contributions

Yunao Zheng: Data curation (lead); Formal analysis (equal); Investigation (lead); Methodology (equal); Software (lead); Validation (lead); Writing – original draft (lead); Writing – review & editing (equal). **Azumi Maekawa**: Software (supporting); Writing – review & editing (supporting). **Yasuaki Monnai**: Conceptualization (lead); Formal analysis (equal); Funding acquisition (lead); Methodology (equal); Project administration (lead); Resources (lead); Software (supporting); Supervision (lead); Writing – original draft (supporting); Writing – review & editing (equal).

DATA AVAILABILITY

The data that support the findings of this study are available from the corresponding author upon reasonable request.

REFERENCES

[1]X. Wang, J. B. Fowlkes, J. M. Cannata, C. Hu, and P. L. Carson, "Photoacoustic imaging with a commercial ultrasound system and a custom probe," Ultrasound Med. Biol. **37**, 484–492 (2011).
[2]C. M. Moran and A. J. W. Thomson, "Preclinical ultrasound imaging—A review of techniques and imaging applications," Front. Phys. **8**, 124 (2020).
[3]J. Ma, X. Ma, and L. Xu, "Optical ultrasound sensing for biomedical imaging," Measurement **200**, 111620 (2022).
[4]A. C. Tam, "Applications of photoacoustic sensing techniques," Rev. Mod. Phys. **58**, 381–431 (1986).
[5]S.-H. Tseng, P. Bargo, A. Durkin, and N. Kollias, "Chromophore concentrations, absorption and scattering properties of human skin *in-vivo*," Opt. Express **17**, 14599–14617 (2009).
[6]M. Li, Y. Tang, and J. Yao, "Photoacoustic tomography of blood oxygenation: A mini review," Photoacoustics **10**, 65–73 (2018).
[7]H. Lee, W. Choi, C. Kim, B. Park, and J. Kim, "Review on ultrasound-guided photoacoustic imaging for complementary analyses of biological systems *in vivo*," Exp. Biol. Med. **248**, 762–774 (2023).
[8]A. Taruttis and V. Ntziachristos, "Advances in real-time multispectral optoacoustic imaging and its applications," Nat. Photonics **9**, 219–227 (2015).
[9]Z. Xu, C. Li, and L. V. Wang, "Photoacoustic tomography of water in phantoms and tissue," J. Biomed. Opt. **15**, 036019 (2010).
[10]T. J. Allen, P. C. Beard, A. Hall, A. P. Dhillon, and J. S. Owen, "Spectroscopic photoacoustic imaging of lipid-rich plaques in the human aorta in the 740 to 1400 nm wavelength range," J. Biomed. Opt. **17**, 061209 (2012).
[11]A. B. E. Attia, G. Balasundaram, M. Moothanchery, U. S. Dinish, R. Bi, V. Ntziachristos, and M. Olivo, "A review of clinical photoacoustic imaging: Current and future trends," Photoacoustics **16**, 100144 (2019).
[12]D. L. Longo, R. Stefania, S. Aime, and A. Oraevsky, "Melanin-based contrast agents for biomedical optoacoustic imaging and theranostic applications," Int. J. Mol. Sci. **18**, 1719 (2017).
[13]J. L. Johnson, J. Shragge, and K. van Wijk, "Nonconfocal all-optical laser-ultrasound and photoacoustic imaging system for angle-dependent deep tissue imaging," J. Biomed. Opt. **22**, 041014 (2017).
[14]E. Dieussaert, R. Baets, H. Jans, X. Rottenberg, and Y. Li, "Non-contact photoacoustic imaging with a silicon photonics-based laser Doppler vibrometer," Sci. Rep. **14**, 22953 (2024).
[15]R. W. Speirs and A. I. Bishop, "Photoacoustic tomography using a Michelson interferometer with quadrature phase detection," Appl. Phys. Lett. **103**, 053501 (2013).
[16]E. Zhang, J. Laufer, and P. Beard, "Backward-mode multiwavelength photoacoustic scanner using a planar Fabry-Perot polymer film ultrasound sensor for high-resolution three-dimensional imaging of biological tissues," Appl. Opt. **47**, 561–577 (2008).
[17]J. L. Johnson, M. Merrilees, J. Shragge, and K. van Wijk, "All-optical extravascular laser-ultrasound and photoacoustic imaging of calcified atherosclerotic plaque in excised carotid artery," Photoacoustics **9**, 62–72 (2018).
[18]T. Stratoudaki, M. Clark, and P. D. Wilcox, "Adapting the full matrix capture and the total focusing method to laser ultrasonics for remote non destructive testing," in *2017 IEEE International Ultrasonics Symposium (IUS)* (IEEE, 2017), pp. 1–4.
[19]G. Rousseau, B. Gauthier, A. Blouin, and J.-P. Monchalin, "Non-contact biomedical photoacoustic and ultrasound imaging," J. Biomed. Opt. **17**, 061217 (2012).
[20]D. George, H. Lloyd, R. H. Silverman, and P. V. Chitnis, "A frequency-domain non-contact photoacoustic microscope based on an adaptive interferometer," J. Biophot. **11**, e201700278 (2018).
[21]J. R. Fincke, C. M. Wynn, R. Haupt, X. Zhang, D. Rivera, and B. Anthony, "Characterization of laser ultrasound source signals in biological tissues for imaging applications," J. Biomed. Opt. **24**, 021206 (2018).
[22]A. Hochreiner, T. Berer, H. Grün, M. Leitner, and P. Burgholzer, "Photoacoustic imaging using an adaptive interferometer with a photorefractive crystal," J. Biophot. **5**, 508–517 (2012).
[23]X. Zhang, J. R. Fincke, C. M. Wynn, M. R. Johnson, R. W. Haupt, and B. W. Anthony, "Full noncontact laser ultrasound: First human data," Light: Sci. Appl. **8**, 119 (2019).
[24]L. Thrane, R. H. Jacobsen, P. Uhd Jepsen, and S. R. Keiding, "Thz reflection spectroscopy of liquid water," Chem. Phys. Lett. **240**, 330–333 (1995).
[25]T. Masaaki, E. Tomoyuki, and I. Ryuji, "Mid-infrared light-induced photoacoustic wave in water and its application," Appl. Phys. Express **16**, 012007 (2023).
[26]K. F. Palmer and D. Williams, "Optical properties of water in the near infrared," J. Opt. Soc. Am. **64**, 1107–1110 (1974).
[27]A. Y. Pawar, D. D. Sonawane, K. B. Erande, and D. V. Derle, "Terahertz technology and its applications," Drug Invent. Today **5**, 157–163 (2013).

[28]M. Tsubouchi, H. Hoshina, M. Nagai, and G. Isoyama, "Plane photoacoustic wave generation in liquid water using irradiation of terahertz pulses," Sci. Rep. **10**, 18537 (2020).
[29]J. Li, Y. Yao, L. Jiang, S. Li, Z. Yi, X. Chen, Z. Tian, and W. Zhang, "Time-domain terahertz optoacoustics: Manipulable water sensing and dampening," Adv. Photonics **3**, 026003 (2021).
[30]W. Wang, L. Huang, H. Zhou, S. Gong, H. Zeng, J. Zhou, Z. Yang, and Y. Zhang, "Low frequency terahertz induced thermoacoustic signal characteristics and its application in solid-state terahertz transmitter power detection," IEEE Trans. Terahertz Sci. Technol. **12**, 673–677 (2022).
[31]T. Hirata, M. Inami, and Y. Monnai, "Sub-terahertz photoacoustic effect enabling broadband ultrasound generation for underwater communication," APL Photonics **8**, 096106 (2023).
[32]L. Jiang, K. Zhang, Y. Yao, J. Liang, J. Li, and Z. Tian, "Frequency-domain terahertz optoacoustics for non-contact quantitative detection of gas, liquid, and solid samples," Opt. Lett. **49**, 490–493 (2024).
[33]Y. Zheng and Y. Monnai, "Non-contact ultrasound sensing platform towards in-vivo applications based on terahertz photoacoustic effect and laser vibrometry," in *2025 International Conference on Mobile and Miniaturized Terahertz Systems (ICMMTS)* (IEEE, 2025), pp. 284–287.
[34]N. Ichikawa and Y. Monnai, "Generating in vivo continuous ultrasound based on sub-terahertz photoacoustic effect," APL Photonics **8**, 086105 (2023).
[35]P. Mohajerani, S. Kellnberger, and V. Ntziachristos, "Frequency domain optoacoustic tomography using amplitude and phase," Photoacoustics **2**, 111–118 (2014).
[36]G. Langer, B. Buchegger, J. Jacak, T. A. Klar, and T. Berer, "Frequency domain photoacoustic and fluorescence microscopy," Biomed. Opt. Express **7**, 2692–2702 (2016).
[37]J. Yao and L. V. Wang, "Sensitivity of photoacoustic microscopy," Photoacoustics **2**, 87–101 (2014).
[38]Y. Iravantchi, Y. Zhang, E. Bernitsas, M. Goel, and C. Harrison, "Interferi: Gesture sensing using on-body acoustic interferometry," in *Proceedings of the 2019 CHI Conference on Human Factors in Computing Systems, CHI '19* (Association for Computing Machinery, New York, 2019), pp. 1–13.
[39]A. B. Coppens, "Simple equations for the speed of sound in neptunian waters," J. Acoust. Soc. Am. **69**, 862–863 (1981).
[40]N. G. Parker and M. J. W. Povey, "Ultrasonic study of the gelation of gelatin: Phase diagram, hysteresis and kinetics," Food Hydrocolloids **26**, 99–107 (2012).
[41]M. M. Nguyen, S. Zhou, J.-l. Robert, V. Shamdasani, and H. Xie, "Development of oil-in-gelatin phantoms for viscoelasticity measurement in ultrasound shear wave elastography," Ultrasound Med. Biol. **40**, 168–176 (2014).
[42]M. O. Culjat, D. Goldenberg, P. Tewari, and R. S. Singh, "A review of tissue substitutes for ultrasound imaging," Ultrasound Med. Biol. **36**, 861–873 (2010).
[43]Japan Ministry of Internal Affairs and Communications, "Radio radiation protection guidelines," 2018.
[44]T. Suzuki, K. Takayama, S. Yamauchi, Y. Imai, and M. Tonouchi, "Measurement of water absorption coefficient using terahertz time-domain spectroscopy," in *2009 34th International Conference on Infrared, Millimeter, and Terahertz Waves* (IEEE, 2009), pp. 1–2.